ACS APPLIED MATERIALS & INTERFACES

Research Article

www.acsami.org

Defect-Induced Enhancement and Quenching Control of Photocurrent in Few-Layer Graphene Photodetectors

Prarthana Gowda, Tushar Sakorikar, Siva K. Reddy, Darim B. Ferry, and Abha Misra*

Department of Instrumentation and Applied Physics, Indian Institute of Science, Bangalore, Karnataka 560012, India

ABSTRACT: A novel approach is presented for achieving an enhanced photoresponse in a few layer graphene (FLG) based photodetector that is realized by introducing defect sites in the FLG. Fabrication induced wrinkle formation in graphene presented a four-fold enhancement in the photocurrent when compared to unfold FLG. Interestingly, it was observed that the addition of few multiwalled carbon nanotubes to an FLG improves the photocurrent by two-fold along with a highly stable response as compared to FLG alone.

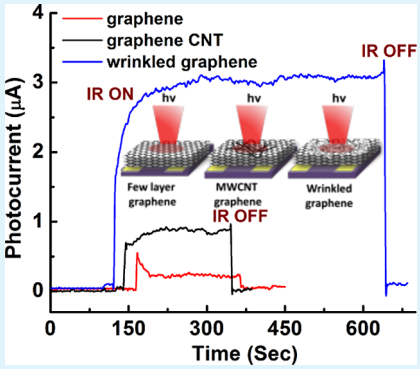

KEYWORDS: *graphene, multiwalled carbon nanotubes, wrinkled graphene, photodetector, photocurrent*

INTRODUCTION

Among the existing two dimensional materials, graphene is gaining much importance due to its exceptional electrical,[1] thermal,[2] mechanical[3] and optical[4] properties that present its potential for a variety of applications in the diverse areas of electronics,[5] sensors,[6,7] optoelectronics,[8] etc. Though graphene is a semimetal, its band gap can be tuned by removing the energetic degeneracy between the sublattices using several methods such as electrostatic or chemical functionalization, etc.[9,10] Moreover, excellent optical properties like the generation of high photocurrent (PC) are achieved using various modification schemes,[11−13] which provided a prospective efficient substitution for the existing photosensitive materials.[14,15] In the optical devices, photoresponsivity is an important parameter for applications in optoelectronics,[16] photodetectors[17] and energy harvesting.[18,19] Therefore, an enhancement in the photoresponsivity and the analysis of associated mechanisms have been attempted in several theoretical[20,21] and experimental[22] studies. These studies reveal that the possible mechanisms may include thermoelectric effect[23,24] due to the presence of temperature gradient and carrier multiplication,[21] and these characteristics are shown to depend upon the number of layers in graphene.[25] These processes are contributed by various scattering phenomena like electron−electron (e−e), electron−phonon (e−p) and phonon−phonon (p−p) scatterings. In order to enhance interaction between the incident radiation and graphene, some forms of defects have been introduced in the carbon lattice. Many researchers have reported an improved photoresponsivity using namely quantum dots,[26,27] suspended graphene,[28] graphene plasmonics[29,30] and graphene nanocomposites.[31,32] A fundamental idea commonly suggested in these studies is to generate more number of scattering sites in order to reduce carrier recombination and facilitate continuous channel for charge carriers, which would eventually enhance and stabilize the PC. Although most of these studies are limited to single layer and bi-layer graphene,[25] few reports have also recently focused on few-layer graphene (FLG).[33] As reported by Mak et al.,[33] the stacked structure of the FLG can assist achieving significant control over its electronic properties. A recent study indicated that a change in the morphology of the FLG could drastically improve the PC by introducing an interlayer of titanium oxide in between the layered graphene that reduces the charge recombination process, thus eliminating the PC decay.[34]

In this work, for the first time an enhanced photoresponse using a wrinkled graphene (WG) is observed when compared to FLG and multi walled carbon nanotubes (MWCNT) dispersed on FLG (MWCNT-G). Wrinkling is an interesting phenomenon ubiquitous to large area growth of graphene, which can appear by many factors like during transfer process,[35] as in our case. It has been shown theoretically[36] and experimentally[37,38] that folding of graphene layers may lead to different processes of electron transport and depending upon the orientation of the fold it may be diffusive or through interlayer tunneling.

The experiments were carried out on above-mentioned samples namely FLG, MWCNT-G and WG for two instances; saturation and cyclical exposures of infrared (IR) radiation. In the case of saturation, IR was exposed until PC reaches a stable value. In the case of cyclical exposure, IR was turned on and off for an interval of 30 s for three cycles. Figure 1a illustrates the

Received: February 10, 2014
Accepted: April 30, 2014
Published: April 30, 2014

   dx.doi.org/10.1021/am500865f | ACS Appl. Mater. Interfaces 2014, 6, 7485−7490

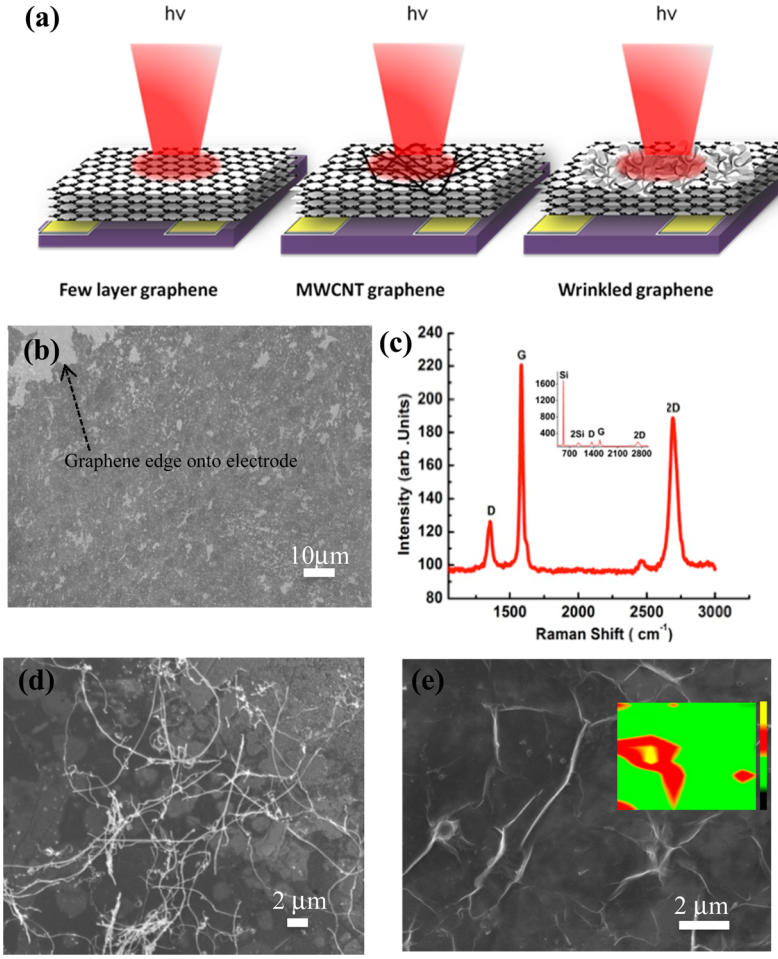

Figure 1. (a) Schematic of the different samples: left to right images are FLG, MWCNT-G and WG, respectively. (b) SEM image of the FLG sample. (c) Raman spectra of the FLG. Inset shows Raman peaks of SiO_2/Si substrate along with FLG Raman spectra. (d) SEM image of the MWCNT-G sample shows the distribution of MWCNT on FLG. (e) SEM image of the WG shows the wrinkles on the FLG. Inset shows Raman G-band intensity map at wrinkle-FLG interface.

schematics of the FLG, MWCNT-G and WG placed between the gold electrodes deposited onto the glass substrate. The left schematic describes the FLG sample without wrinkles or defects, whereas the middle schematic shows the MWCNT dropcasted on FLG and the right image represents WG sample. The scanning electron micrograph (SEM) of the as-grown graphene (a detailed growth procedure can be found in the experimental section) transferred between the electrodes is shown in Figure 1b and a dark contrast in the image shows an edge of the FLG lying onto the gold electrode.

Raman spectroscopy was conducted to verify the quality of the graphene. Figure 1c elucidates the Raman spectra of the FLG, which depicts the appearance of G and 2D modes at 1588 and 2686 cm^{-1}. To estimate the number of layers in graphene the ratio of the G peak intensity and Si peak is calculated as suggested in refs 39 and 40. The ratio I_G/I_{Si} was found to be ~0.14, which indicates that the number of layers in our sample is less than four.

Images d and e in Figure 1 illustrate SEM images of the distribution of the MWCNT on FLG and WG in between the electrodes, respectively. The presence of wrinkles in the graphene is confirmed by Raman G-band mapping of the WG as shown in the inset of Figure 1e, which reveals a sharp difference in the color intensity. In the intensity map, green color region shows the unfolded graphene, whereas the red and yellow colors show the folded portion of the graphene.[38]

RESULTS AND DISCUSSION

Figure 2 shows the photo response during the saturation and cyclical experiments on the FLG, MWCNT-G and WG samples. The saturation and cyclical exposure observation carried out on FLG are illustrated in panels a and b in Figure 2, respectively. PC is shown to generate instantaneously as soon as FLG is exposed to IR (Figure 2a). The value of maximum generated PC depends on IR power and it increases with the increase in the incident IR power. The maximum PC values are 781, 550, 284 and 112 nA at 200, 150, 100 and 65 mW, respectively. Interestingly, the PC decreases after a prolonged exposure (~100 s) of IR radiation. From the experimental data it is apparent that the decay rate of PC depends on the number of incident photons and a higher decay rate is observed at higher incident IR powers. Inset in Figure 2a shows a decay curve obtained at 150 mW power that is fitted with two different slopes; Slope-1 shows a fast cooling, whereas slope-2 illustrates a gradual cooling of photo generated carriers,[41] the overall response is fitted with the following relation to evaluate the range for the time constants

$$I_{PC} = \alpha e^{(-t/\tau_1)} + \beta e^{(-t/\tau_2)} + A \quad (1)$$

dx.doi.org/10.1021/am500865f | ACS Appl. Mater. Interfaces 2014, 6, 7485−7490

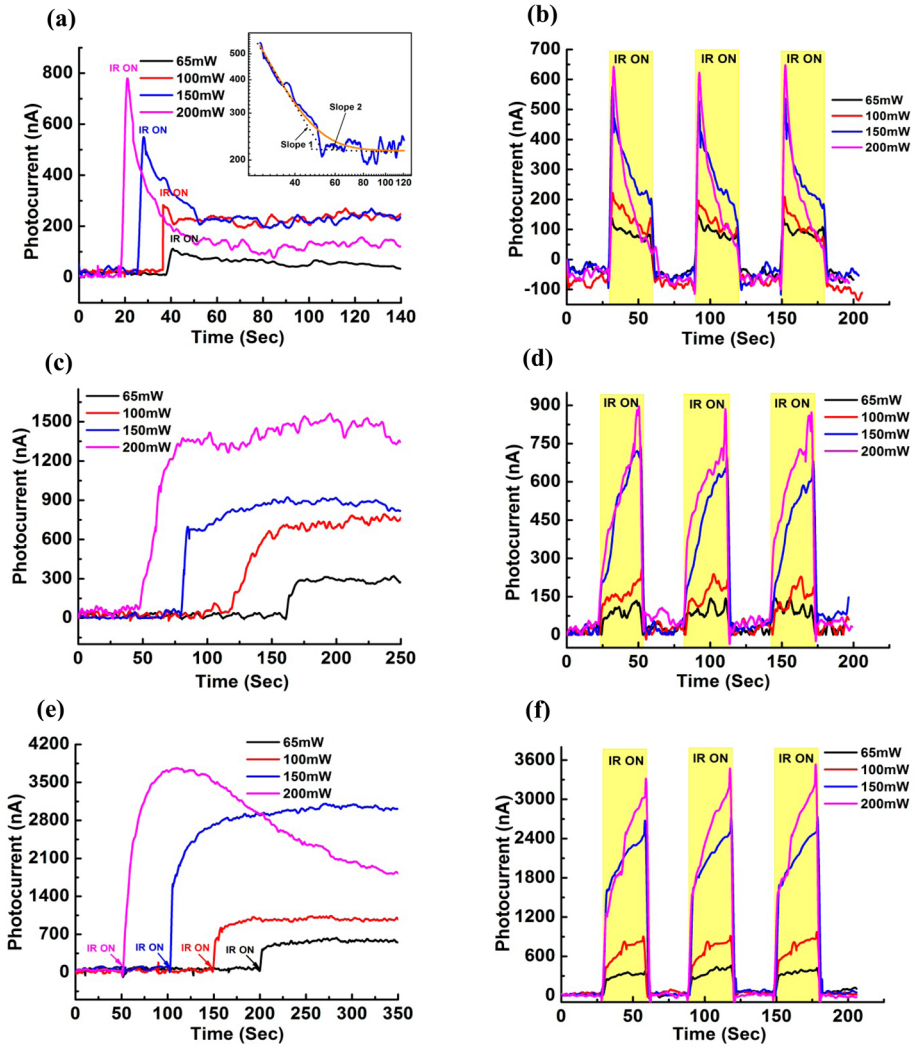

Figure 2. Saturation and cyclical PC generation of (a, b) FLG sample, respectively; (c, d) MWCNT-G, respectively; (e, f) WG, respectively. Inset to (a) shows the two different decay rates of the generated PC for 150 mW.

where I_{PC} represents photocurrent, time constants τ_1 and τ_2 lie between ~5 ± 2 and ~55 ± 3 s for all incident powers, A is a constant and α, β values are dependent on the incident power of the IR source. After decay, PC stabilizes to a saturation value as is inferred in Figure 2(a) and this current stabilization is clearly shown to depend on the IR power. In the saturation state, the final PC reduces by 86, 61, 31 and 26% of the peak value at incident IR powers of 200, 150, 100 and 65 mW, respectively. Thus, it is clear that the percentage decay value increases with the increase in the incident optical power. There are several mechanisms for this decrease, which includes e−e, e−p scattering,[20] charge recombination,[42] Auger recombination and impact ionization.[43] The explanation for the drop in PC after a continuous IR exposure is difficult to state clearly, as several of the aforementioned phenomena can coexist. However, our results can clearly be correlated with an increase in the temperature gradient[20] within different layers of FLG, which in the case of monolayer graphene is a direct function of the laser power[23] as $P_{in} \propto \Delta T$, where P_{in} is the incident IR power and ΔT is the temperature gradient. However, in our case since there is an increase in the number of layers, this relation can be modified to $P_{in} \propto \Delta T^{r}$ where r is a function of number of layers present in FLG, hence $r > 1$ in our case. Therefore, for the higher incident powers (150 and 200 mW), the electron may cool down quickly within a few picoseconds,[44] whereas at lower power (65 and 100 mW), this cooling rate decreases by the order of three.[44] Fast relaxation of photo-excited carriers is attributed to the e−e scattering,[20] which increases with increasing laser power. For the lower power (lower temperature gradient), the acoustic phonon scattering is dominant whereas for the higher power (higher temperature gradient) it is optical phonon scattering,[44] which contribute to the charge recombination. Figure 2b illustrates a dependence of PC generation on cyclical exposure of the incident radiation when IR was exposed for a short period of time for 30 s only, contrary to a prolonged exposure until saturation of PC. The magnitude of maximum PC in all three cycles remains constant for all the respective incident powers, which confirms the photoelastic nature of the sample. At all incident powers during IR exposure, PC decays and the decay rate is observed to decrease with the lowering in IR power, as will be discussed later.

MWCNT-G device is also tested for the saturation and cyclic responses as are shown in panels c and d in Figure 2, respectively. A higher PC is generated than FLG at all incident powers, which remains constant for a prolonged (~150 s) IR exposure as opposed to the FLG device. In this case, the generated PCs for 200, 150, 100 and 65 mW incident IR

dx.doi.org/10.1021/am500865f | ACS Appl. Mater. Interfaces 2014, 6, 7485−7490

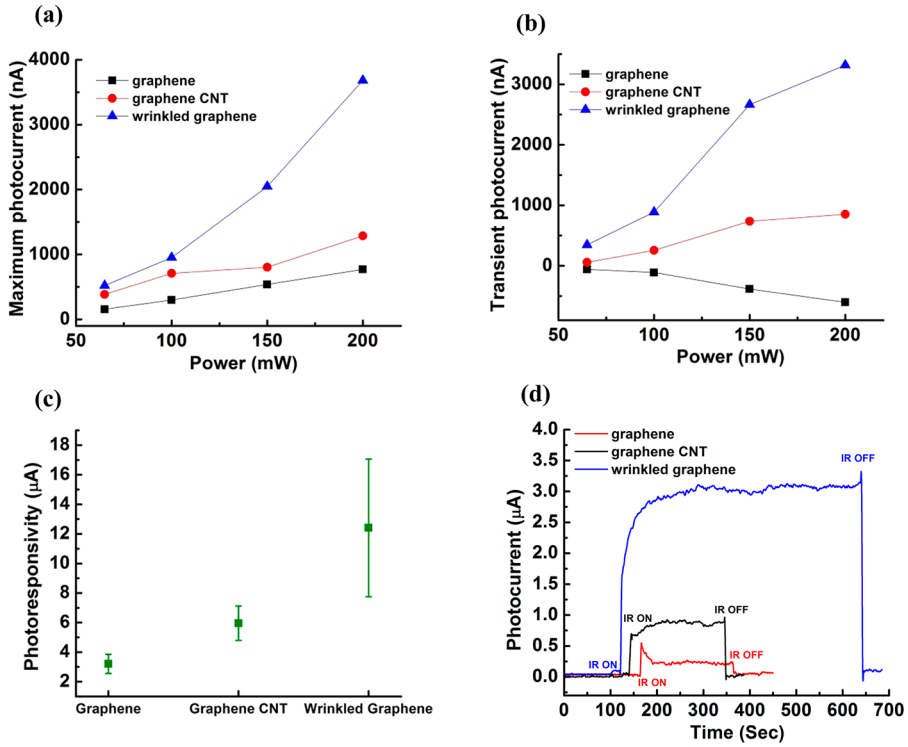

Figure 3. (a) Maximum PC generated during the saturation for different powers and samples. (b) Change in the PC during IR exposure of 30 s for different powers and different samples. (c) Average photoresponsivity of different powers for the different samples (d) Comparison of the different samples response during the saturation for the power of 150 mW.

powers were 1369, 869, 760 and 306 nA, respectively. These values are two-fold higher than in the case of the FLG device; This may be attributed to an increase in the photo carrier generation sites due to random network of MWCNT. In this case, the generated PC is collected and amplified by the graphene layer, which is placed in between the metal electrodes. A highly stable response can be ascribed to interconnected and randomly dispersed MWCNT network onto the FLG that leads to a higher absorption of incident photons,[45] thus larger number of photo generated carriers. The interface between the MWCNT and the FLG provides a Schottky barrier potential of ~0.09 eV.[46] Thus, the generated excitons need much lower energy to cross this barrier and hence largely contribute to PC. Because MWCNT forms a random network onto FLG, it lowers the rate of PC generation by 20 times as compared to that of FLG to reach the saturation state, which can be attributed to diffusive photoconduction in MWCNT.[47] The increase in the photo response of MWCNT-G can be given by the expression in eq 2, which is a combination of an initial experimental rise followed by saturation in PC

$$I_{PC} = ke^{(t/\tau_3)} + B \quad (2)$$

where k and B are constants, t is the time of exposure and τ_3 a time constant, calculated as ~20 ± 2 s for all powers.

Figure 2d shows the cyclical measurements of PC for the photoelastic response of MWCNT-G at all incident powers as similar to that of FLG. However, PC is shown to increase gradually during 30 s IR exposure, unlike FLG. A similar trend can be observed at all incident powers. The maximum value of PCs measured for the power of 200, 150, 100 and 65 mW are 889, 708, 237 and 140 nA, respectively. Thus, again a direct relation between incident power and generated PC can be elucidated.

Panels e and f in Figure 2 illustrate the photo response from the WG device. The maximum generated PC for highest IR power of 200 mW in WG is found to be two and four fold higher than that of FLG and MWCNT-G devices, respectively. It is worth noticing that the photo response decays after reaching its maximum value at 200 mW unlike at lower powers. These results suggest that the photo response of WG stabilizes at its maximum value only upto 150 mW and then upon further increasing the power it starts decaying possibly between 150 to 200 mW. At maximum power of 200 mW, PC reaches to its peak value at 3756 nA and then decays to saturate at 1847 nA, which is 49% of the maximum value. The maximum PCs generated for the powers viz. 150, 100 and 65 mW are 2994, 983 and 524 nA, respectively and hence reveals a direct relation between generated PC and the incident IR power.

The possible reason for the stable responses until 150 mW of IR power can be attributed to an increase in the number of graphene layer that leads to a gradual profile of the temperature gradient across the sample unlike in the case of FLG, thus minimizing the probability of optical phonon bottleneck and eventually quenching of the photogenerated carriers.

The reversible photo response of WG is monitored through cyclic exposure of IR radiation. Figure 2f confirms the photo elastic response of WG. PC is shown to gradually increase and reaches to a maximum value of 3441, 2712, 928 and 418 nA for the incident powers of 200, 150, 100 and 65 mW, respectively, within an interval of 30 s. Generation of higher PC in WG presents an interesting aspect in analysis as it is composed of folded layers of the FLG that present it as a three-dimensional structure because of the increased thickness.[38] This folding may also induce some curvature that can change the bonding configuration in graphene and hence affects its conductance.[37] However, in the case of 200 mW power, it is possible that the

creation of excitons have overcome the number of unoccupied electronic states available in the layered structure, leading to an optical phonon bottleneck[41] and hence causing a decay of PC after reaching the peak value. Interestingly, unlike FLG, the relaxation of excitons is not sudden but is revealed to occur gradually because of an increased number of layers.

Figure 3a shows a comparison among the different graphene devices during saturation experiment as mentioned earlier for their maximum generated PC at different powers. It is interesting to notice that at higher incident powers (>100 mW) among all three devices, WG shows a highly nonlinear increase in PC, whereas the photo response from MWCNT-G and FLG increases linearly with the increasing power.

Figure 3b illustrates a transient response of PC for an interval of 30 s of IR exposure. It is clear that the WG and the MWCNT-G reveal a rise in PC with an increase in IR power, which is represented in positive transient PC in the graph.

However, the FLG showed decay in PC with an increase in the incident IR power, which is demonstrated as negative PC in the graph. It is illustrated in the figure that rise and decay of the transient PC increases with the incident IR power. It is elucidated that decay for the FLG and rise for the MWCNT-G and the WG in transient PC is highest for 200 mW IR power.

Figure 3c shows a comparison of photoresponsivity of the above-mentioned three devices during saturation experiment. The WG shows a highest photoresponsivity followed by the MWCNT-G and the FLG with a larger deviation. The reason for this deviation could be related to a nonlinear increase in PC with the incident power. Figure 3d reveals the saturation pattern for three devices at 150 mW incident power to clearly demonstrate a dependence of PC generation on the morphology of the graphene. The FLG reveals a sharp rise and then an exponential decay during IR exposure, whereas the MWCNT-G and the WG illustrate a gradual increase and then stabilization in the PC generation. A study on device speed on all the three samples was performed and it is concluded that the FLG reaches the maximum current value in 2.53, 2.96, 3.04 and 3.241 s; whereas for MWCNT-G it is 11.24, 44.44, 68.72 and 111.44 s and finally for the WG shows 26.56, 43, 123.5 and 56.6 s for 65, 100, 150 and 200 mW, respectively; these results suggest that though FLG showed a less stability, a faster response can be observed than both of the MWCNT-G and the WG samples.

CONCLUSION

In summary, we report an enhanced and stable PC generated by inducing defects in FLG using a very simple yet efficient method. We experimentally studied the effects of wrinkles and presence of MWCNT on the PC generation in FLG. The presence of MWCNT on FLG enhances the stability but lacked at photoresponsivity compared to that of the WG. Whereas the WG was found to be highly efficient in both stability and photoresponsivity except for higher power. The exact mechanism of PC generation in WG is still unclear and requires further study. However, the future work can be directed towards engineering the wrinkles as well as density variation of MWCNT or their alignment to enhance the PC yield.

EXPERIMENTAL PROCEDURES

Graphene and Carbon Nanotube Growth Processes. FLG was grown by chemical vapor deposition (CVD) on copper (Cu) substrate of area 1.2 cm^2 with a thickness of 25 μm. Initially, the reaction chamber was flushed with argon (Ar) gas flowing at 800 sccm (standard cubic centimeters per minute) for 25 min, while the temperature of the reaction chamber reaches to 980 °C. Thereafter, the substrate was annealed for 1 h in the presence of Ar and hydrogen (H_2) gases flowing at the rates of 800 and 300 sccm, respectively. Methane was injected into the chamber for 3 min to grow graphene onto the substrate.

Bundles of MWCNT were grown by CVD and the growth process involves the solution of toluene and ferrocene mixed in a 0.02 ratio and this solution was then vaporized before reaching a reaction zone. The reaction zone was maintained at 825 °C and the vaporized solution was flown using Ar as a carrier gas flowing at a rate of 800 sccm.[48] MWCNT were grown vertically (length 40 μm) on the silicon dioxide substrate and were later scraped off from the substrate.

Fabrication of Graphene Photodetector. The gold electrodes of 50 nm thickness with a separation of 90 μm were deposited on a glass substrate by using radio frequency sputtering and then FLG was transferred in between the electrodes. MWCNT were dispersed in a 10 ml of chloroform by sonicating 2.2 mg of MWCNT for 7 h. These dispersed MWCNT were drop casted using microsyringe on FLG that is already placed between the electrodes. Figure 1d illustrate SEM image of the distribution of MWCNT on FLG in between the electrodes. Wrinkles were formed during the transfer process of graphene from the Cu substrate on to the middle of the metal electrode gap. These wrinkles are evident from the SEM image shown in Figure 1e.

IR Source and Electrical Measurements. Infrared (IR) laser (Opto-Link Corporation Limited) of 1550 nm wavelength, whose output was passed through an optical fiber of diameter ~125 μm with a core diameter of ~8 μm; was used for the IR exposure to the graphene samples. The PC measurements were carried out using Agilent B1505A power device analyzer. Electrical measurements on the samples were performed using the tungsten probes of tip diameter 20 μm.

Raman Spectroscopy and Mapping. The presence of FLG was confirmed by Raman spectroscopy by using high-resolution Raman and fluorescence spectrometer (Horiba Jobin Yvon LabRAM). The laser source of wavelength of 532 nm and power 0.2 mW was used for spectroscopy study. Raman mapping using the same instrument with a laser power of 0.5 mW characterized the wrinkles in the sample. The mapping is carried out for the area of 10 × 10 μm^2 with the distance between the consecutive points as 1 μm.

AUTHOR INFORMATION

Corresponding Author

*E-mail: abha@isu.iisc.ernet.in.

Notes

The authors declare no competing financial interest.

ACKNOWLEDGMENTS

A.M. acknowledges partial funding support from Center for Infrastructure, Sustainable Transportation and Urban Planning (CiSTUP). We thank MNCF (Micro and Nano Characterization Facility), CENSE (Centre for Nano Science and Engineering), IISc (Indian Institute of Science) for providing the characterization facility.

REFERENCES

(1) Novoselov, K. S.; Geim, A. K.; Morozov, S. V.; Jiang, D.; Zhang, Y.; Dubonos, S. V.; Grigorieva, I. V.; Firsov, A. A. Electric Field Effect in Atomically Thin Carbon Films. *Science* **2004**, *306*, 666−669.

(2) Shahil, K. M. F.; Goyal, V.; Balandin, A. A. Thermal Properties of Graphene: Applications in Thermal Interface Materials. *ECS Trans.* **2011**, *35*, 193−199.

(3) Liu, Y.; Xie, B.; Zhang, Z.; Zheng, Q.; Xu, Z. Mechanical Properties of Graphene Papers. *J. Mech. Phys. Solids* **2012**, *60*, 591−605.

(4) Liu, M.; Yin, X.; Ulin-Avila, E.; Geng, B.; Zentgraf, T.; Ju, L.; Wang, F.; Zhang, X. A Graphene-Based Broadband Optical Modulator. *Nature* **2011**, *474*, 64−67.
(5) Schwierz, F. Graphene Transistors. *Nat. Nanotechnol.* **2010**, *5*, 487−496.
(6) Schedin, F.; Geim, A. K.; Morozov, S.V.; Hill, E. W.; Blake, P.; Katsnelson, M. I.; Novoselov, K. S. Detection of Individual Gas Molecules Adsorbed on Graphene. *Nat. Mater.* **2007**, *6*, 652−655.
(7) Guo, C. X.; Lu, Z. S.; Lei, Y.; Li, C. M. Ionic Liquid−Graphene Composite for Ultratrace Explosive Trinitrotoluene Detection. *Electrochem. Commun.* **2010**, *12*, 1237−1240.
(8) Vakil, A.; Engheta, N. Transformation Optics Using Graphene. *Science* **2011**, *332*, 1291−1294.
(9) Craciun, M. F.; Russo, S.; Yamamoto, M.; Tarucha, S. Tuneable Electronic Properties in Graphene. *Nano Today* **2011**, *6*, 42−60.
(10) Craciun, M. F.; Khrapach, I.; Barnes, M. D.; Russo, S. Properties and Applications of Chemically Functionalized Graphene. *J. Phys. Condens. Matter* **2013**, *25*, 423201−423223.
(11) Song, S.; Chen, Q.; Jina, L.; Sun, F. Great Light Absorption Enhancement in a Graphene Photodetector Integrated with a Metamaterial Perfect Absorber. *Nanoscale.* **2013**, *5*, 9615−9619.
(12) Fang, Z.; Liu, Z.; Wang, Y.; Ajayan, P. M.; Nordlander, P.; Halas, N. J. Graphene-Antenna Sandwich Photodetector. *Nano Lett.* **2012**, *12*, 3808−3813.
(13) Furchi, M.; Urich, A.; Pospischil, A.; Lilley, G.; Unterrainer, K.; Detz, H.; Klang, P.; Andrews, A. M.; Schrenk, W.; Strasser, G.; Mueller, T. Microcavity-Integrated Graphene Photodetector. *Nano Lett.* **2012**, *12*, 2773−2777.
(14) Xia, F.; Mueller, T.; Lin, Y.; Valdes-Garcia, A.; Avouris, P. Ultrafast Graphene Photodetector. *Nat. Nanotechnol.* **2009**, *4*, 839−843.
(15) Loomis, J.; Panchapakesan, B. Large Photocurrents in Single Layer Graphene Thin Films: Effects of Diffusion and Drift. *Nanotechnology* **2012**, *23*, 265203−265215.
(16) Bonaccorso, F.; Sun, Z.; Hasan, T.; Ferrari, A. C. Graphene Photonics and Optoelectronics. *Nat. Photonics* **2010**, *4*, 611−622.
(17) Mueller, T.; Xia, F.; Avouris, P. Graphene Photodetectors for High-Speed Optical Communications. *Nat. Photonics* **2010**, *4*, 297−301.
(18) Fan, G.; Zhu, H.; Wang, K.; Wei, J.; Li, X.; Shu, Q.; Guo, N.; Wu, D. Graphene/Silicon Nanowire Schottky Junction for Enhanced Light Harvesting. *ACS Appl. Mater. Interfaces* **2011**, *3*, 721−725.
(19) Dhiman, P.; Yavari, F.; Mi, X.; Gullapalli, H.; Shi, Y.; Ajayan, P. M.; Koratkar, N. Harvesting Energy from Water Flow Over Graphene. *Nano Lett.* **2011**, *11*, 3123−3127.
(20) Kim, R.; Perebeinos, V.; Avouris, P. Relaxation of Optically Excited Carriers in Graphene. *Phys. Rev. B* **2011**, *84*, 075449−075454.
(21) Winzer, T.; Knorr, A.; Malic, E. Multiplication of Photo-Excited Carriers in Graphene. *Nano Lett.* **2010**, *10*, 4839−4843.
(22) Zhang, Y.; Liu, T.; Meng, B.; Li, X.; Liang, G.; Hu, X.; Wang, Q. J. Broadband High Photoresponse from Pure Monolayer Graphene Photodetector. *Nat. Commun.* **2013**, *4*, 1811.
(23) Xu, X.; Gabor, N. M.; Alden, J. S.; Zande, A. M.; McEuen, P. L. Photo-Thermoelectric Effect at a Graphene Interface Junction. *Nano Lett.* **2010**, *10*, 562−566.
(24) Withers, F.; Bointon, T. H.; Craciun, M. F.; Russo, S. All-Graphene Photodetectors. *ACS Nano* **2013**, *7*, 5052−5057.
(25) Zhu, W.; Perebeinos, V.; Freitag, M.; Avouris, P. Carrier Scattering, Mobilities and Electrostatic Potential in Mono-, Bi- and Tri-Layer Graphenes. *Phys. Rev. B* **2009**, *80*, 35402−35420.
(26) Klekachev, A. V.; Nourbakhsh, A.; Asselberghs, I.; Stesmans, A. L.; Heyns, M. M.; Gendt, D. S. Graphene Transistors and Photodetectors. *Electrochem. Soc. Interface* **2013**, 63−68.
(27) Guo, C. X.; Yang, H. B.; Sheng, Z. M.; Lu, Z. S.; Song, Q. L.; Li, C. M. Layered Graphene/Quantum Dots for Photovoltaic Devices. *Angew. Chem. Int. Ed.* **2010**, *49*, 3014−3017.
(28) Freitag, M.; Low, T.; Avouris, P. Increased Responsivity of Suspended Graphene Photodetectors. *Nano Lett.* **2013**, *13*, 1644−1652.
(29) Koppens, F. H. L.; Chang, D. E.; de Abajo, F. J. G. Graphene Plasmonics: A Platform for Strong Light-Matter Interactions. *Nano Lett.* **2011**, *11*, 3370−3377.
(30) Ju, L.; Geng, B.; Horng, J.; Girit, C.; Martin, M.; Hao, Z.; Bechtel, H. A.; Liang, X.; Zet, A.; Shen, Y.R.; Wang, F. Graphene Plasmonics for Tunable Terahertz Metamaterials. *Nat. Nanotechnol.* **2011**, *6*, 630−634.
(31) Du, A.; Sanvito, S.; Li, Z.; Wang, D.; Jiao, Y.; Liao, T.; Sun, Q.; Ng, Y. H.; Zhu, Z.; Amal, R.; Smith, S. C. Hybrid Graphene and Graphitic Carbon Nitride Nanocomposite: Gap Opening, Electron−Hole Puddle, Interfacial Charge Transfer, and Enhanced Visible Light Response. *J. Am. Chem. Soc.* **2012**, *134*, 4393−4400.
(32) Son, D. I.; Yang, H. Y.; Kim, T. W.; Park, W. I. Photoresponse Mechanisms of Ultraviolet Photodetectors Based on Colloidal ZnO Quantum Dot-Graphene Nanocomposites. *Appl. Phys. Lett.* **2013**, *102*, 021105−021108.
(33) Mak, K. F.; Sfeir, M. Y.; Misewich, J. A.; Heinz, T. F. The Evolution of Electronic Structure in Few-Layer Graphene Revealed by Optical Spectroscopy. *Proc. Natl. Acad. Sci. U.S.A.* **2010**, *107*, 14999−15004.
(34) Yang, H.; Guo, C.; Guai, G. H.; Song, Q.; Jiang, S. P.; Li, C. M. Reduction of Charge Recombination by an Amorphous Titanium Oxide Interlayer in Layered Graphene/Quantum Dots Photochemical Cells. *ACS Appl. Mater. Interfaces* **2011**, *3*, 1940−1945.
(35) Liu, N.; Pan, Z.; Fu, L.; Zhang, C.; Dai, B.; Liu, Z. The Origin of Wrinkles on Transferred Graphene. *Nano Res.* **2011**, *4*, 996−1004.
(36) Kim, K.; Lee, Z.; Malone, B. D.; Chan, K. T.; Aleman, B.; Regan, W.; Gannett, W.; Crommie, M. F.; Cohen, M. L.; Zettl, A. Multiply Folded Graphene. *Phys. Rev. B* **2011**, *83*, 245433−245441.
(37) Xu, K.; Cao, P.; Heath, J. R. Scanning Tunneling Microscopy Characterization of the Electrical Properties of Wrinkles in Exfoliated Graphene Monolayers. *Nano Lett.* **2009**, *9*, 4446−4451.
(38) Zhu, W.; Low, T.; Perebeinos, V.; Bol, A. A.; Zhu, Y.; Yan, H.; Tersoff, J.; Avouris, P. Structure and Electronic Transport in Graphene Wrinkles. *Nano Lett.* **2012**, *12*, 3431−3436.
(39) Jhang, S.; Craciun, M.; Schmidmeier, S.; Tokumitsu, S.; Russo, S.; Yamamoto, M.; Skourski, Y.; Wosnitza, J.; Tarucha, S.; Eroms, J.; Strunk, C. Stacking-Order Dependent Transport Properties of Trilayer Graphene. *Phys. Rev. B* **2011**, *84*, 161408(R).
(40) Koh, Y. K.; Bae, M.-H.; Cahill, D. G.; Pop, E. Reliably Counting Atomic Planes of Few-Layer Graphene ($n > 4$). *ACS Nano* **2011**, *5*, 269−274.
(41) Strait, J. H.; Wang, H.; Shivaraman, S.; Shields, V.; Spencer, M.; Rana, F. Very Slow Cooling Dynamics of Photoexcited Carriers in Graphene Observed by Optical-Pump Terahertz-Probe Spectroscopy. *Nano Lett.* **2011**, *11*, 4902−4906.
(42) Limmer, T.; Feldmann, J.; Como, E. D. Carrier Lifetime in Exfoliated Few-Layer Graphene Determined from Intersubband Optical Transitions. *Phys. Rev. Lett.* **2013**, *110*, 217406−217411.
(43) Song, J. C. W.; Rudner, M. S.; Marcus, C. M.; Levitov, L. S. Hot Carrier Transport and Photocurrent Response in Graphene. *Nano Lett.* **2011**, *11*, 4688−4692.
(44) Bistritzer, R.; MacDonald, A. H. Electronic Cooling in Graphene. *Appl. Phys. Lett.* **2009**, *102*, 206410−206414.
(45) Kaul, A. B.; Coles, J. B.; Eastwood, M.; Green, R. O.; Bandaru, P. R. Ultra-High Optical Absorption Efficiency from the Ultraviolet to the Infrared Using Multi-Walled Carbon Nanotube Ensembles. *Small* **2013**, *9*, 1058−1065.
(46) Cook, B. G.; French, W. R.; Varga, K. Electron Transport Properties of Carbon Nanotube−Graphene Contacts. *Appl. Phys. Lett.* **2012**, *101*, 153501−153503.
(47) Sarker, B. K.; Arif, M.; Stokes, P.; Khondaker, S. I. Diffusion Mediated Photoconduction in Multi-Walled Carbon Nanotube Films. *J. Appl. Phys.* **2009**, *106*, 074307−074311.
(48) Reddy, S. K.; Suri, A.; Misra, A. Influence of Magnetic Field on the Compressive Behavior of Carbon Nanotube with Magnetic Nanoparticles. *Appl. Phys. Lett.* **2013**, *102*, 241919−241923.